

# The nonlinear ultrasound needle pulse

P. Ted Christopher

71 Azalea Road, Rochester, New York 14620, USA

Kevin J. Parker<sup>a)</sup>

Departments of Electrical & Computer and of Biomedical Engineering, University of Rochester, Rochester, New York 14627, USA

(Received 8 February 2018; revised 25 June 2018; accepted 26 July 2018; published online 21 August 2018)

Recent work has established an analytical formulation of broadband fields which extend in the axial direction and converge to a narrow concentrated line. Those unique (needle) fields have their origins in an angular spectrum configuration in which the forward propagating wavenumber of the field ( $k_z$ ) is constant across any  $z$  plane for all of the propagated frequencies. A 3 MHz-based, finite amplitude distorted simulation of such a field is considered here in a water path scenario relevant to medical imaging. That nonlinear simulation had its focal features compared to those of a comparable Gaussian beam. The results suggest that the unique convergence of the needle pulse to a narrow but extended axial line in linear propagation is also inherited by higher harmonics in nonlinear propagation. Furthermore, the linear needle field's relatively short duration focal pulses, and the asymptotic declines of its radial profiles, also hold for the associated higher harmonics. Comparisons with the Gaussian field highlight some unique and potentially productive features of needle fields. © 2018 Acoustical Society of America. <https://doi.org/10.1121/1.5050519>

[YJ]

Pages: 861–871

## I. INTRODUCTION

A new class of propagation invariant fields has been formulated based on the principle of a wideband source excitation configured through the angular spectrum such that all components propagate with equal phase in the forward propagating direction (Parker and Alonso, 2016). Analytic solutions were obtained for a one-dimensional (1D) source, then for an axial symmetric source, and for a pulsed version of the field. The free space solution has some unusual properties including vanishing group velocity and a convergence of all energy to a narrow central line as a spatial and temporal peak, or crescendo; hence the appellation “needle pulse.” Dynamic visualizations are given online in links found in Parker and Alonso (2016); these demonstrate the convergence of the waveform to the crescendo and subsequent divergence. In the needle pulse there is no focusing in the conventional sense and the excitation of a source that is composed of 1D or two-dimensional (2D) array elements can be realized by sampling bounded input waveforms that are expressed in analytical form. The needle pulse can be considered to fall within a class of nearly propagation-invariant beams (Hefner and Marston, 1999; Hernández-Figueroa *et al.*, 2008; Brunet *et al.*, 2009; Baresch *et al.*, 2016).

In this paper, we provide an introduction to the nonlinear acoustic characteristics of the needle pulse fields and their implementation in radial symmetric ultrasound transducers. The needle pulse field is compared against more conventional Gaussian beams which have been studied in optics and acoustics (Du and Breazeale, 1985, 1986, 1987; Wen

and Breazeale, 1988; Lu *et al.*, 1994; Hamilton and Blackstock, 1998b; Ding and Liu, 1999; Huang and Breazeale, 2006; Marston, 2011; Parker *et al.*, 2017).

Our investigations employ numerical techniques. As a background, we summarize some of the main approaches. For cases of sound beams propagating predominantly in one direction, the Westervelt equation (Westervelt, 1963) can be reduced to the Khokhlov-Zabolotskaya-Kuznetsov (KZK) equation (Zabolotskaya and Khokhlov, 1969; Hamilton and Blackstock, 1998a), which has also been described as an augmentation of the Burgers' equation (Hamilton and Blackstock, 1998a) and been shown to agree well with experimental results (Canney *et al.*, 2010).

Several algorithms have been developed to solve the KZK equation (Aanonsen *et al.*, 1984; Lee and Hamilton, 1995; Cleveland *et al.*, 1996; Pishchal'nikov *et al.*, 1996; Varslot and Taraldsen, 2005; Jing and Cleveland, 2007; Dagrau *et al.*, 2011; Tripathi *et al.*, 2018). According to Qiao *et al.* (2016): “In order to capture full diffraction a number of approaches have been reported. One approach is to relax the parabolic approximation either in the frequency domain (Christopher and Parker, 1991a) or the time domain (Tavakkoli *et al.*, 1998). A second is to solve the Westervelt equation directly (Hallaj and Cleveland, 1999). A third approach is to solve the underlying nonlinear hydrodynamic equations, for example, with high order finite-difference time domain methods (Ginter *et al.*, 2002) or a  $k$ -space approach (Treeby *et al.*, 2012). Full diffraction models typically have very high computational costs but modeling some nonlinear ultrasound problems can be tractable with the help of parallel and cluster computing (Yuldashev and Khokhlova, 2011; Kenji *et al.*, 2012). Finite element methods (FEMs) have also been adopted to simulate nonlinear

<sup>a)</sup>Electronic mail: kevin.parker@rochester.edu

wave propagation and they are well suited to handling complex geometries such as occur in the body (Wojcik *et al.*, 1995; Hoffelner *et al.*, 2001).” The commercial FEM software PZFLEX (Weidlinger Associates, Inc., Mountain View, CA) is now available for these cases (Qiao *et al.*, 2016). In this research the propagation substep approach is taken as described in Sec. II. That approach has successfully modeled a variety of continuous and pulses sources, including in high intensity scenarios (Christopher and Parker, 1991a; Christopher, 1994, 1997, 2005).

## II. THEORY

The linear solution for the needle pulse pressure  $p$  in 2D (radial symmetry) using a Gaussian spectral width  $\delta$  is:

$$p(r, z, t) = c_0 \frac{\exp\left[-k_L \sqrt{r^2 - c_0^2(t - iq)^2}\right] \exp[ik_L z]}{k_L \sqrt{r^2 - c_0^2(t - iq)^2}} \times \exp\left[-\frac{\delta^2}{2} \left(z + i \sqrt{r^2 - c_0^2(t - iq)^2}\right)^2\right], \quad (1)$$

where  $r = (x^2 + y^2)^{1/2}$ ,  $x$  and  $y$  are the transverse coordinates,  $z$  is the axial coordinate,  $k_L$  is the lowest (minimum) wavenumber propagated,  $c_0$  is the speed of sound, and  $t$  is time. These solutions have a full width of approximately  $2(c_0^2 t^2 + q^2)^{1/2}$ , the parameter  $q$  regulates how spatially localized these solutions are at  $t = 0$  (Parker *et al.*, 2017).

Note that  $t = 0$  does not correspond to the initial time but to the time at which the field is most concentrated spatially. In theory, the excitation must exist for all negative times. The parameter  $q$  determines the bandwidth of the spectrum used and, therefore, how narrow the field becomes at  $t = 0$ .

To generate this field, the simplest approach is to apply the broadband source distribution at plane  $z = 0$  as simply the real part of Eq. (1) with  $z = 0$ , starting at a large negative time and working through and including  $t = 0$ , when the crescendo occurs. However, since the solution is derived from plane to plane angular spectra, source excitation can be implemented at any plane  $z < 0$ . For arrays in ultrasound applications, spatial samples of Eq. (1) would constitute the source excitation signals (Parker *et al.*, 2017).

The needle pulse has some interesting properties. Its factorization of the dependence in  $z$  as a simple exponential means that the pulse has vanishing group velocity. The pressure field as it develops toward the “crescendo” at  $t = 0$  exhibits spherical curvature over an extended axial range, then a convergence followed by a reverse spherical curvature. For visualizations, see the online movies of reference (Parker and Alonso, 2016).

### A. The linear diffractive substep

The linear effects of diffraction, attenuation, refraction, and reflection are extensively covered in an earlier paper (Christopher and Parker, 1991b); the model’s linear substep

derived from that presentation—along with an updated procedure—will be summarized here. A multiharmonic, acoustic normal velocity (or pressure) field in a plane can be diffracted  $\Delta z$  forward by convolving each of the constituent harmonic fields with an appropriate point spread function,

$$h_n(\Delta z, r) = -\frac{1}{2\pi} \frac{\Delta z}{d^2} \left( jnk - \frac{1}{d} \right) e^{jnk d}, \quad (2)$$

where  $r$  is the radial coordinate,  $n$  represents the harmonic index, and  $d = \sqrt{r^2 + \Delta z^2}$ . Direct sampling of the  $h_n(\Delta z, r)$  functions results in a correct implementation of the (Fourier) convolution theorem. Alternatively, convolution can be computed using direct sampling of the analytical Hankel transform of  $h_n$ ,

$$H_n(\Delta z, R) = \begin{cases} \exp\left[j2\pi\Delta z \sqrt{(nf/c)^2 - R^2}\right], & |R| \leq nf/c, \\ \exp\left[-2\pi\Delta z \sqrt{R^2 - (nf/c)^2}\right], & |R| > nf/c. \end{cases} \quad (3)$$

In the earlier presentation an efficient scheme involving dynamic limits placed on the inclusion of the  $H_n(\Delta z, R)$  samples (and thus multiplications) was discussed. Those limits involved the propagation geometry-given spatial frequency content of those  $H_n(\Delta z, R)$  samples. In an update beyond that approach, it has been found that utilizing a full direct sampling of  $H_n(\Delta z, R)$  values is more accurate and computationally simpler. This current approach generously allows for  $H_n$  terms up to and including some evanescent samples  $|R| > nf/c$ . This scheme accurately describes each  $\Delta z$  linear advancement and then a periodic spatial (cosine) windowing of the edges of the propagating harmonic fields limits convolutional artifacts. This still results in reduced multiplications since these operations can be terminated after a few evanescent  $|R| > nf/c$  terms.

On a general note, if non-axis symmetric sources must be propagated, this substep (in either a nonlinear or linear computation) can be generalized to accommodate them by exchanging the current Hankel transform (and radial grid structure) for a 2D fast Fourier transform (FFT) (and a square grid). Frequency-dependent attenuation can be included in the diffractive substep by combining a power law multiplicative factor with the point spread function  $h_n$ . Alternatively, the plane wave-oriented propagation of the  $H_n$  (or angular spectrum) approach can be supplemented with a power law-based multiplicative (plane wave) attenuation factor (Christopher and Parker, 1991b). In either case the multiplicative factor looks like  $e^{-\alpha f^b d}$ , where  $f$  is frequency,  $d$  is distance, and  $\alpha$  and  $b$  describe the power law relationship.

### B. The nonlinear substep

In general, the acoustic normal velocity field at a point  $r_i$  in a plane given by  $z_i$  can be represented by a multiharmonic waveform. If this normal velocity waveform represented a plane wave traveling in the  $z$  direction, then the

effect of nonlinearity on the waveform in traveling over a distance  $\Delta z$  could be computed using the frequency domain solution to Burgers' equation (FDSBE). The attenuation term of the FDSBE is not considered here as attenuation is computed in the linear diffractive substep. In this way, the model accounts for the nonlinear effect by supplementing each  $\Delta z$  linear substep with a  $\Delta z$  nonlinear plane wave displacement of the field. The order of the substeps is reversible, but the results here utilized the linear substep first, followed by the nonlinear substep.

The nonlinear plane wave substep then consists of applying the FDSBE (minus the attenuation term) to each multi-harmonic radial field sample that has been output by the most recent linear substep. The  $i$ th iteration of the FDSBE algorithm can be written

$$u_n(z + \Delta z, i) = u'_n(z + \Delta z, i) + j \frac{\beta \pi f \Delta z}{2c^2} \left( \sum_{k=1}^{n-1} k u'_k u'_{n-k} + \sum_{k=n}^N k u'_k u'^*_{n-k} \right),$$

$$n = 1, 2, \dots, N, \quad (4)$$

where  $\beta$  is the nonlinear parameter  $1 + (B/2A)$ ,  $f$  is the fundamental frequency, and  $u_n(z + \Delta z, i)$  denotes the  $n$ th term in an  $N$  term complex Fourier series describing the temporal normal velocity waveform at the  $i$ th radial field sample in the plane  $z + \Delta z$ . Note that the output of the linear substep  $u'_n(z + \Delta z, i)$  has been abbreviated within the bracketed summations by dropping the  $z + \Delta z, i$  specification. This computation is repeated for each of the  $N$  radial samples ( $i = 0, 1, \dots, N - 1$ ). The first summation within the large parentheses represents the accretion of the  $n$ th harmonic by nonlinear combination of other harmonics that have a sum frequency of  $nf$ . The second summation, with conjugation, can be interpreted as a depletion of the  $n$ th harmonic to other harmonics with a difference of frequency  $nf$ .

Note that the above formulation is consistent with the original one, but for the computations here pressure  $p$  was used to represent the focusing fields. In that case  $(\beta \pi f \Delta z)/(2c^2)$  is replaced by  $(\beta \pi f \Delta z)/(2c^3 \rho)$ .

### III. METHODS

The original single harmonic source formulation had to be extended to allow for multi-harmonic pulses. This was done by replacing the algorithm's single harmonic input with the multi-harmonic, FFT-based description of the desired ultrasonic source pulses.

Another subtle aspect of the original algorithm had to be updated for the current work. That aspect involved the computation of the local directivity of the field [Eq. (4) in [Christopher and Parker \(1991a\)](#)]. That computation was motivated by the recognition that the field at some radial position is not in general propagating normally to its planar grid representation. Without a correction for this offset directivity, the nonlinear (plane wave-oriented) substep would inaccurately represent the distance over which finite amplitude distortion accrued. It could also misrepresent the true

amplitude of a radial sample's harmonics in the case of a normal velocity representation ( $u_n$ ) of the field. In that case actual amplitude associated with normal velocity propagating through a grid point is  $|u_n|/\cos(\theta)$  and the pending propagation distance is  $\Delta z/\cos(\theta)$ , where  $\theta$  is the angular offset (or directionality) of the local wavefront relative to the norm of the planar grid. In the trivial case of  $\theta = 0$  radians, the local wavefront is parallel to the propagation grid and there is no need for a correction.

Our original treatment of this complication involved the utilization of the fundamental harmonic's phase change in the radial dimension. That radial phase change was in turn used to compute the directionality of the local ultrasonic field and thus better estimate the corresponding propagation distance associated with the pending  $\Delta z$  nonlinear advancement of the field, and also to modify the harmonic amplitudes input into the FDSBE for the case of a normal velocity representation.

An update to this directivity computation was necessitated by the broadband nature of the needle source. The associated field's requirement of a constant phase change between planes imposes a rise in center frequency with increasing off-axis distance within the needle's focusing field. That radial transition to higher center frequencies in turn means that any single frequency can only accurately represent the direction of the field over a limited radial extent. To accommodate the demands of this broadband field, the updated algorithm allows for the specification of a sequence of constituent harmonics. Then, at any given radial field sample, the constituent harmonic with the largest amplitude is identified. Next, the remaining specified harmonics which have amplitudes of at least 1/60th of that maximum amplitude were selected. Each of those significant harmonics (as output by the linear substep) has its rate of radial phase change  $S$  calculated along the propagation radius, depicted here for the  $n$ th harmonic,

$$S[u'_n(z, i)] = \frac{d}{dr} \left[ \tan^{-1} \left( \frac{\text{Im}[u'_n(z, r)]}{\text{Re}[u'_n(z, r)]} \right) \right]. \quad (5)$$

The  $S$  quantity physically represents the spatial frequency associated with a plane wave of the  $n$ th harmonic intercepting the grid at a particular angle  $\theta$  [this geometric idea was considered at some length in [Christopher and Parker \(1991b\)](#)]. Then each of these  $S$  values was converted into a desired angular quantity  $\theta[u'_n(z, i)]$  by

$$\sin(\theta[u'_n(z, i)]) = S[u'_n(z, i)]/\max(S_n), \quad (6)$$

where  $\max(S_n)$  equals the maximum spatial frequency associated with the  $n$ th harmonic intercepting the grid. This occurs when that harmonic travels parallel to the grid and it equals  $f_n/c_n$ , where  $f_n$  and  $c_n$  are the frequency and sound speed of the  $n$ th harmonic. Finally, the specified significant harmonics have their  $\sin(\theta)$  values combined into a simple linear amplitude-weighted summation. That resulting  $\sin(\theta)$  summation value is converted to a  $\cos(\theta)$  value which was used to correct for directivity in the FDSBE

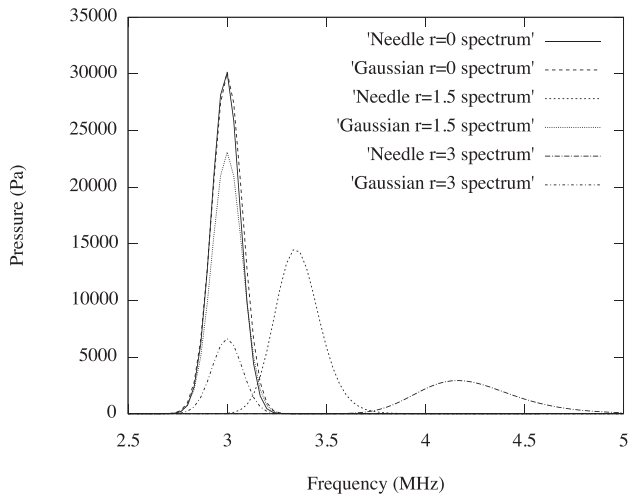


FIG. 1. Axially-symmetric, needle and Gaussian source plane ( $z = -3.0$  cm) pressure spectra. The Gaussian source was defined with a center frequency of 3 MHz, an on-axis RMS intensity of  $1 \text{ W/cm}^2$ , and temporal and spatial apodization  $\sigma$  values of  $0.48 \mu\text{s}$  and  $0.58 \text{ cm}$ , respectively. The needle source was defined using Eq. (1) with a center frequency of 3 MHz,  $s = 0.3$ , and  $q = 0.2$ . The radial extent of both sources was 3 cm, the temporal extent of their pulse representations was  $30 \mu\text{s}$ , and the medium was water. Spectra are shown for the  $r = 0.0$ ,  $r = 1.5$ , and  $r = 3.0$  cm positions.

substep. Unlike any single harmonic-based estimate, the resulting summation-based directivity estimate appeared to offer stable and accurate directivity values for the focusing needle field.

### A. Respective fields

The two focal pressure sources had radial extents of 3 cm and also focal lengths of 3 cm. The specified media parameters were those of water which included  $c = 0.15 \text{ cm}/\mu\text{s}$ ,  $\rho = 1 \text{ g/cm}^3$ ,  $\alpha = 0.00025 \text{ Np/cm}$ ,  $b = 2$ , and nonlinear constant  $\beta = 3.5$ . The needle source was obtained by utilizing Eq. (7) in Parker *et al.* (2017) with the parameters  $z = -3 \text{ cm}$ ,  $q = 0.2$ ,  $s = 0.3$ , and had an on-axis center frequency of 3 MHz. The corresponding Gaussian source was

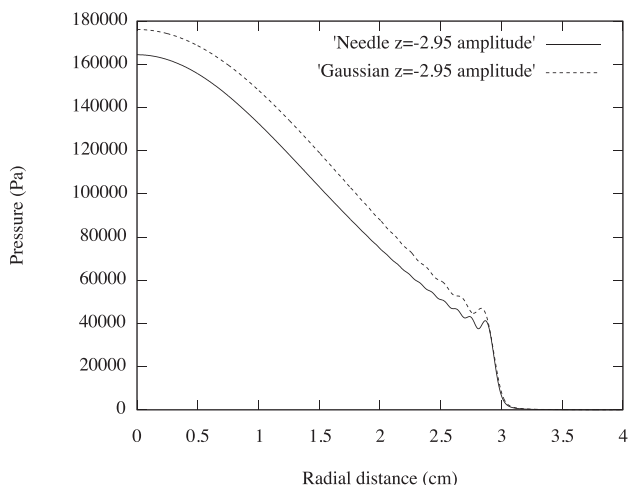


FIG. 2. The near source,  $z = -2.95$  cm, peak pressure profiles propagated by the needle and Gaussian sources. The needle source was scaled to produce the same linearly propagated, focal ( $z = 0.0$ ,  $r = 0.0$ ) pressure value as the Gaussian source.

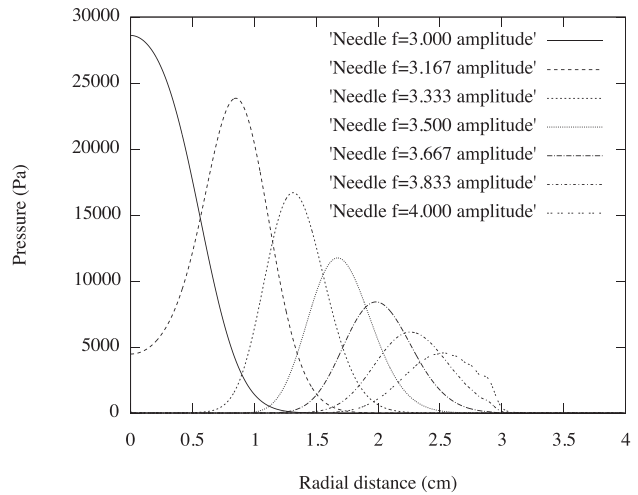


FIG. 3. The near source,  $z = -2.95$  cm, pressure amplitude profiles for the needle sources' harmonics 90, 95, 100, 105, 110, 115, and 120 from the pulse's frequency domain representation. These harmonics correspond to frequency values of 3.000, 3.167, 3.333, 3.500, 3.667, 3.833, and 4.000 MHz. The phase changes in these profiles were collectively used to estimate the directionality in order to accurately estimate the effects of finite amplitude distortion within the focused needle field.

specified using a Gaussian apodized 3 MHz cosine pulse. The Gaussian apodization parameter  $\sigma_G = 0.48 \mu\text{s}$  was selected to match the on-axis specifics of the needle pulse. That 3 MHz Gaussian pulse was in turn Fourier-transformed and then had its constituent harmonics spread out and spherically-focused along the source plane radius. That Gaussian source harmonic description was then spatially apodized with a Gaussian constant  $\sigma_G = 0.58 \text{ cm}$  applied, to match the form of the needle source's amplitude profile.

Note that because the comparison began with the output of the needle field equation, the resulting source description

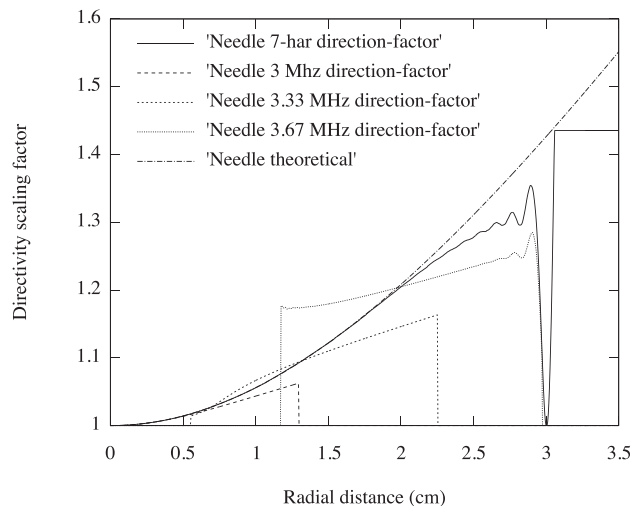


FIG. 4. The directivity-based nonlinear scaling factor  $1/\cos \theta$  for the near source,  $z = -2.95$  cm, needle pressure field. The solid curve was based on a weighted sum of the directivity angles associated with 7 harmonics (or frequencies) in the propagating field. The next three dashed curves represent single frequency (3.000, 3.33, and 3.67 MHz) based estimates. The final dashed curve represents a spherically focused or theoretical based estimate. Near the edge of the focusing field—and outwards of the edge—there is irregular phasing as the edge of the focal field transitions to a diverging field. A ceiling was added to the directivity algorithm in part to limit these irregular values.

was a pressure description of finite extent. That pressure description in turn had to be scaled up in order to produce meaningful amplitudes for the desired finite amplitude comparison. The way this was accomplished was to take a linear propagation of the Gaussian source, which was anchored to an on-axis root-mean-square (RMS) intensity of  $1 \text{ W/cm}^2$ , out to the  $z = 0.0 \text{ cm}$  focus and then identify the peak pulse amplitude there. The needle source radial representation was then scaled so that its linear peak focal amplitude matched that of the Gaussian source. In this way two roughly equivalent sources were obtained and could then be utilized for a finite amplitude comparison.

The specifics of the propagation grid was that it utilized 3000 samples across a radial extent of 12 cm. The corresponding sampling rate was 250 samples per cm and that corresponded to the Nyquist frequency of an 18.75 MHz wave propagating in water. The  $z$  increment used was 0.01 cm for the first 2 cm and then a smaller increment of 0.005 cm for the next 2 cm. This smaller step size was motivated by the larger finite amplitude effects expected in the focal region. The temporal grid used to represent the pulses was 1024 samples across  $30 \mu\text{s}$ , providing incremental frequency coverage from 0.03 up to 17.06 MHz

(the latter being below the Nyquist-given limit of the grid representation). The 7 harmonics specified for the directivity calculation were harmonics 90, 95, 100, 105, 110, 115, and 120. These harmonics corresponded to 3,  $3.1\bar{6}$ ,  $3.3\bar{3}$ , 3.5,  $3.6\bar{6}$ ,  $3.8\bar{3}$ , and 4 MHz, respectively.

Figures 1 and 2 depict some relevant source plane specifics. Figure 1 shows the corresponding source spectra for the two sources at the inner and outer positions of  $r = 0.0$ ,  $r = 1.5$ , and  $r = 3.0 \text{ cm}$ . Of note here is the shift of the outer needle spectrum to a center frequency of over 4 MHz as well as the broadening of that spectrum. The needle equation implicitly defines not only increasing center frequencies off-axis, but also a shortening of those pulses.

The Gaussian source on the other hand simply reduces their amplitudes and—not shown here—shifts the phases in order to maintain a spherical focus. In Fig. 2, the corresponding source radii pulse peak amplitudes are shown. Since the needle source utilizes additional high frequency content—minimally affected by water’s minimal absorption—it offers a little more efficient focusing here. The Gaussian source thus is almost 10% higher in its source amplitude profile.

Figure 3 shows the radial profiles from  $z = -2.95 \text{ cm}$  of the seven harmonics chosen for the directivity algorithm.

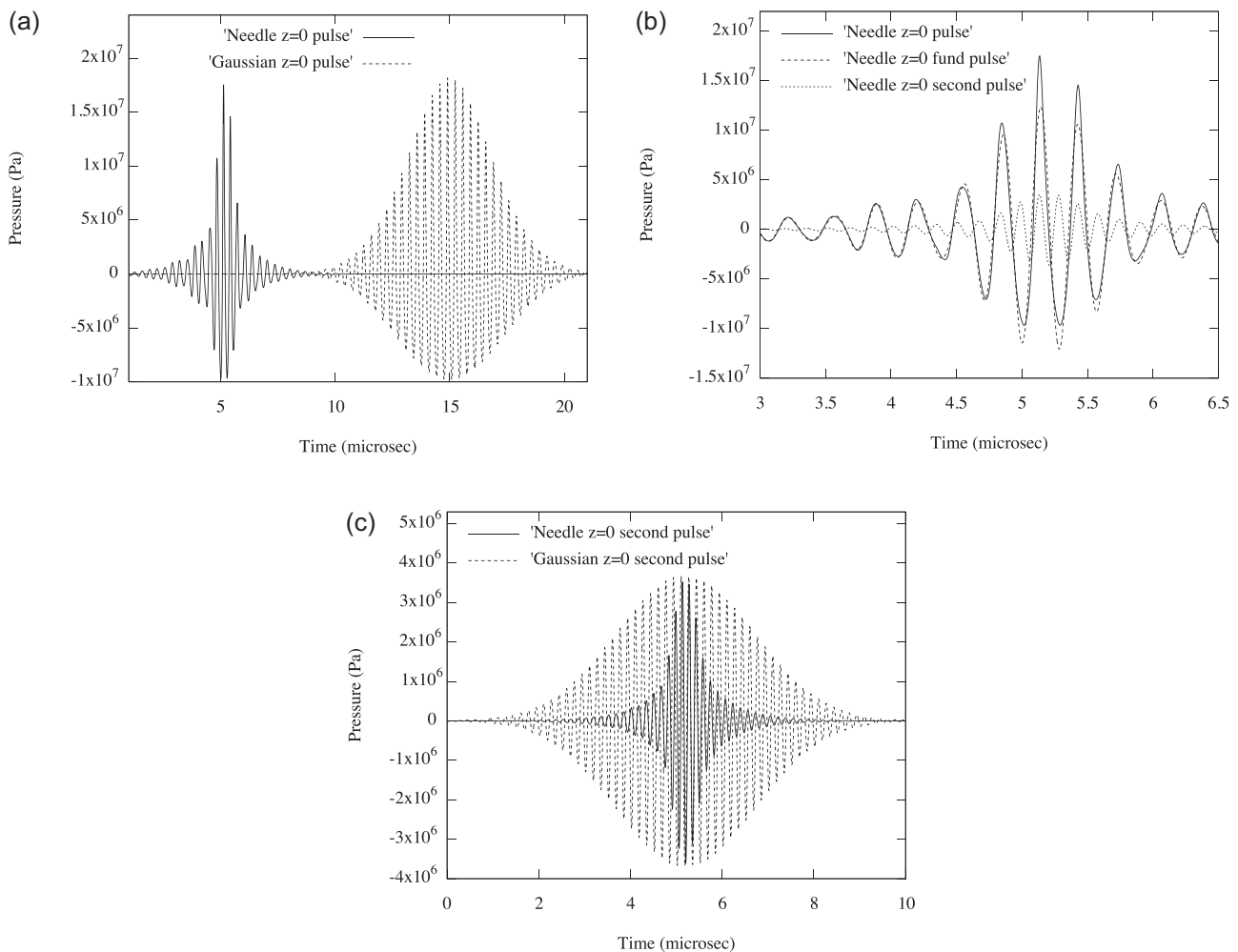


FIG. 5. The focal needle and Gaussian pulses. Note the shorter duration of the needle pulses. (a) Pulses constructed using all 512 harmonics from the nonlinear propagation. (b) Focal needle pulses constructed using all of the harmonics, those associated with the fundamental harmonic bandwidth (harmonics or frequencies 79–162), and those associated with the second harmonic bandwidth (harmonics 165–264). (c) The needle and Gaussian second harmonic bandwidth focal pulses.

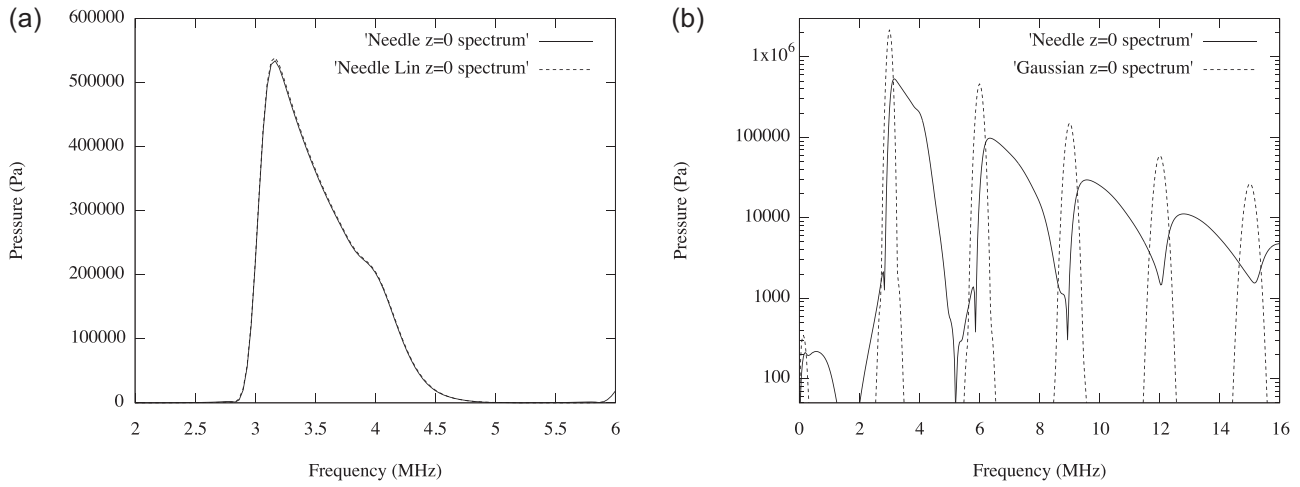


FIG. 6. The focal needle and Gaussian spectra from linear and nonlinear computations. (a) Overlay of the linearly propagated fundamental bandwidth and the corresponding nonlinearly propagated result. Note the minimal losses in the nonlinear result. (b) A log-scaled overlay of the needle and Gaussian focal nonlinear spectra. Note the broadband nature of the needle source's harmonic bands.

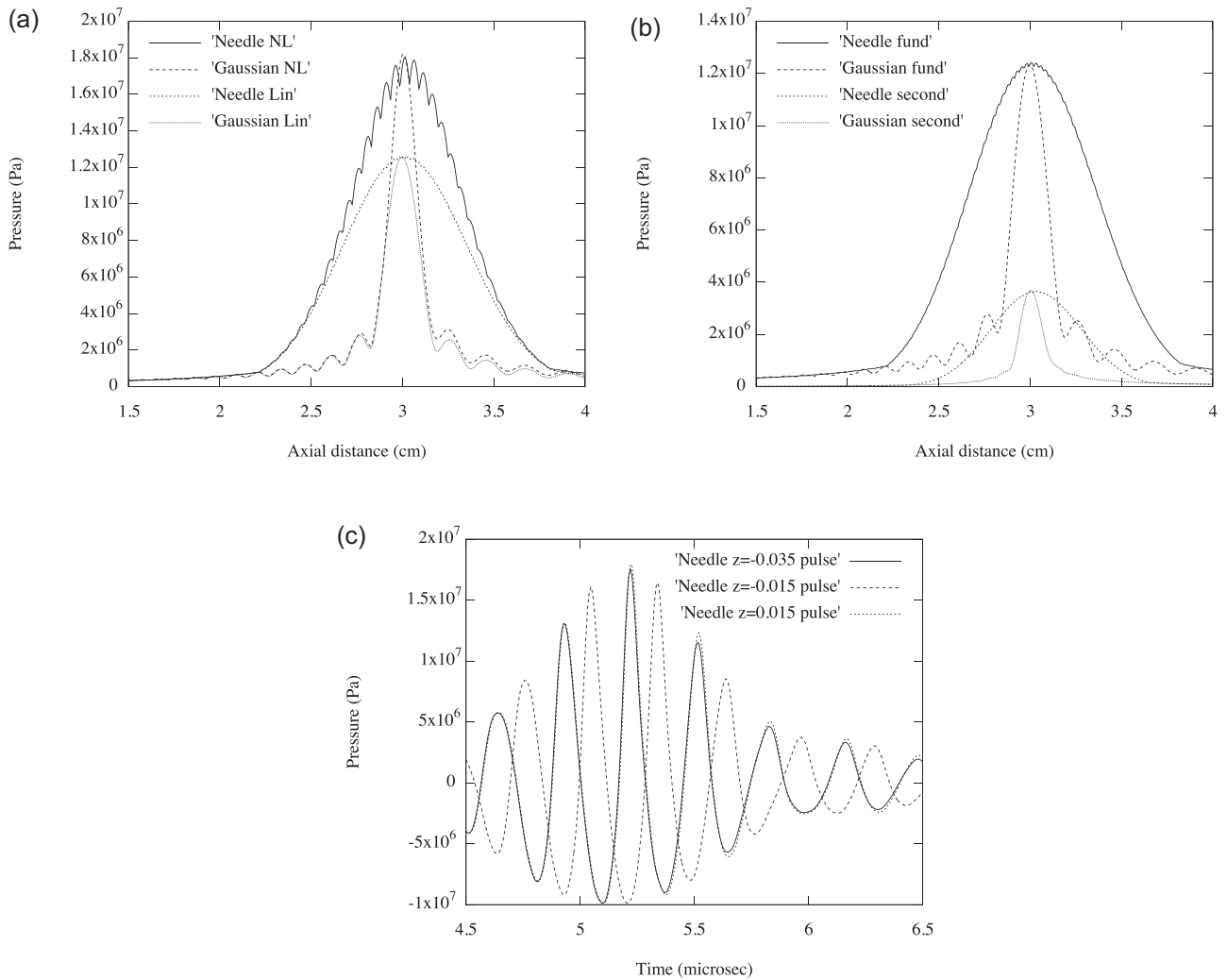


FIG. 7. The axial peak-pulse curves for the needle and Gaussian sources. (a) Results from the linear and nonlinear computations. Both utilized all of the propagating harmonics. (b) The corresponding nonlinear results from the fundamental and second harmonic bands. (c) Focal nonlinear needle pulses at  $z = -0.035$ ,  $z = -0.015$ , and  $z = 0.015$  cm. The first and last of these were separated by 0.05 cm, which equals the wavelength of 3 MHz in water. They were thus similar.

Note that each has its own relatively narrow radial band of significant amplitudes. These seven harmonics were chosen since those amplitude bands extend across the  $r = 0$  to  $r = 3$  cm radii. That coverage in turn offered good estimates across the face of this broadband converging field. The Gaussian field, on the other hand, was everywhere centered on 3 MHz frequency content, and thus the corresponding single harmonic provided the desired directivity estimates.

Figure 4 depicts the directivity-based nonlinear factor  $1/\cos(\theta)$  for the near source,  $z = -2.95$  cm, needle pressure field. The smooth, finest dashed curve shows the theoretical or spherically focused-based directivity scaling factor. The solid curve estimate was based on the previously described, weighted summation of the directivities of seven harmonics. The next three dashed curves represent single harmonic (3.000, 3.333, and 3.667 MHz) based estimates. Toward the edge of the focusing field (and beyond) the directivity exhibits irregular estimates. These derive from the finite extent of the source and the associated edge effects. A ceiling was placed on the irregularity of such estimates and that ceiling was the directivity factor associated with the angle of focusing required at the edge of the source. In Fig. 4 that value is visible and it is about 1.43. For the most part,

concern about this compromise was minimal as the associated field amplitudes are small and outside of the focusing region of the beam.

Figures 5(a)–5(c) then plot the resulting finite amplitude distortion-computed focal pulses. In Fig. 5(a) note the shorter duration of the needle pulse. The broadband-oriented needle equation effectively provides for a pulse concentration in the focal region. Also, both needle and Gaussian waveforms are asymmetric with positive/negative peak pressures exceeding a ratio of 1.5 at the time of crescendo,  $t = 0$ . In Fig. 5(b) several needle focal pulses are shown. Those pulses were constructed using the full nonlinear spectrum [as in Fig. 5(a)], the fundamental harmonic bandwidth, and also the second harmonic bandwidth. Again note how short the full and fundamental harmonics-based results are in comparison to the Gaussian pulse shown in Fig. 5(a). Also shown in Fig. 5(b) is the corresponding second harmonic bandwidth pulse. In Fig. 5(c), the needle's second harmonic bandwidth-based focal pulse is again shown along with that from the Gaussian field. The needle's second harmonic pulse is similarly much shorter than that of the equivalent Gaussian result. Thus the destructive interference noted above appears to extend to the second harmonics' focal performance. An

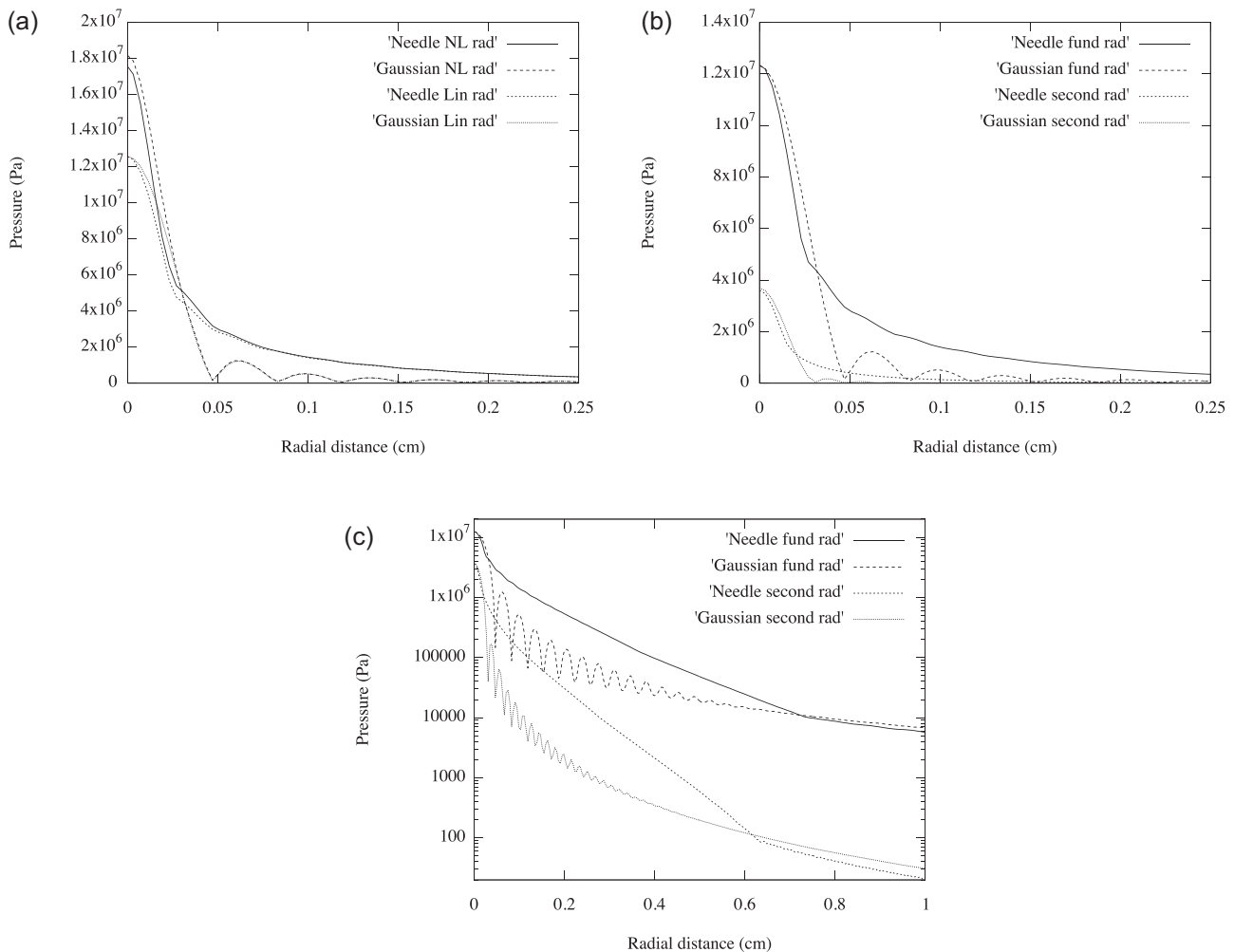


FIG. 8. The focal plane ( $z = 0.0$  cm) radial peak-pulse amplitude profiles for the needle and Gaussian sources. (a) Results from the linear and nonlinear computations. (b) The corresponding peak profiles from the fundamental and second harmonic bands. (c) The log-scaled depiction of the corresponding peak profiles from the fundamental and second harmonic bands. Note the longer radial extent depicted in (c).

additional note here is that the focus on the fundamental and second harmonic bandwidths—here and henceforth—is motivated by their relevance to contemporary ultrasonic imaging.

Next, Figs. 6(a) and 6(b) consider the corresponding focal spectra. Figure 6(a) depicts the fundamental bandwidth of the needle’s focal pulse as computed with and without nonlinearity. The linear spectrum is very similar to the nonlinear spectrum and this is due to the minimal losses experienced from the fundamental band in the nonlinear propagation which did not produce a shock. Figure 6(b) shows the corresponding nonlinear focal spectra in a logarithmic format. The Gaussian spectra are as expected with its higher harmonic narrowband nature. The needle spectra show the broadband nature of its focal behavior. In fact the fundamental portions of that spectra broadly represents an integral description of the broadband source. The increasing higher frequency content in that focal fundamental band corresponds to the contributions from the rising center frequency content in the needle’s off-axis pulses. That focal broadband nature is, in turn, also present in the higher harmonics.

Figures 7(a) and 7(b) show the focal peak axial amplitudes for the needle and Gaussian fields. The respective

lower curves represent the linearly propagated peak amplitudes achieved along the axis. The needle curve is longer in contrast to the corresponding focal pulse lengths considered earlier. Thus, although the needle source produces much shorter focal pulse lengths, it also extends the range over which those short focal pulses maintain significant amplitudes. Next, the respective higher axial amplitude curves in Fig. 7(a) present the corresponding nonlinear results. In both cases those peak curves were computed using the full range of propagating harmonics. The increased heights are derived from the increased positive pressures produced by finite amplitude distortion along the axis in the focal region. The bumpy surface of the needle’s nonlinear peak curve derives from the dynamics in the short needle pulse. In particular, as a local peak maximum fades out, the subsequent peak overtakes it and pushes toward a new maximum amplitude. In Fig. 7(b) the corresponding axial peak amplitude curves associated with the needle’s respective fundamental and second harmonic bands are plotted. Here again the form of the second harmonic bandwidth reflects the form of the associated fundamental results. Finally, Fig. 7(c) depicts the needle’s on-axis pulses at  $z = -0.035$ ,  $z = -0.015$ , and  $z = 0.015$  cm. Notice that the first and last pulses are very similar, and this is due to them being 0.05 cm apart which is

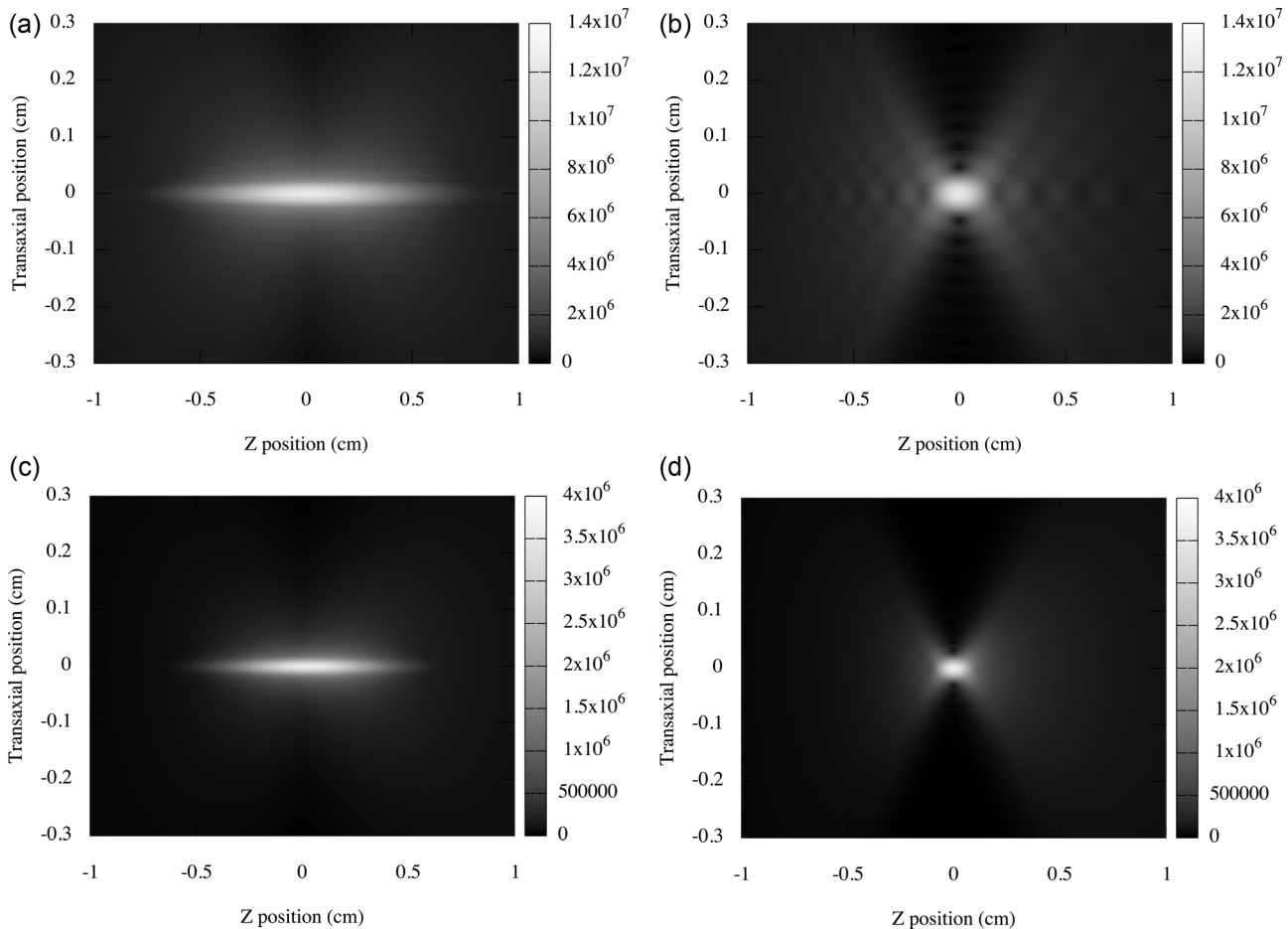


FIG. 9. The transaxial, peak-pulse amplitude planar results for the needle and Gaussian sources. All computations utilized the nonlinear model, but all figures here are linearly scaled. (a) The planar peak pressure amplitude result computed from the needle field’s fundamental band. (b) The corresponding result from the Gaussian’s fundamental band. (c) The planar peak amplitude computed from the needle’s second harmonic band. (d) The corresponding result from the Gaussian’s second harmonic band.

the distance of one 3 MHz wavelength. The peak dynamic depicted between the outer and middle pulses here is the basis for the nonlinear bumpy axial peak profile shown in Fig. 7(a). That is because changes in the distribution of the pulse's positive peaks produces a small variation in the axial peak profile.

Figures 8(a)–8(c) show the focal radial peak amplitude results from the two sources. In Fig. 8(a) the corresponding linear and nonlinearly propagated radial profiles are presented. The nonlinear results utilized the full harmonic range. The lower pair of curves, bearing the linear results, reflects a relationship somewhat analogous to the earlier axial peak curves. The broadband needle source has an almost exponential asymptotic decay away from the central lobe. The narrowband Gaussian linear result, on the other hand, drops faster off-axis. This may reflect the inherent advantages with a single center frequency focal field, in that such fields are better able to achieve destructive interference away from their focal peak. The corresponding nonlinear curves reveal the concentrated boost in peak focal pressures near the axis for both sources. Figure 8(b) depicts the corresponding fundamental and second harmonic band-based results. Note that in both harmonic band cases, the needle result is narrower in the inner portion of the main lobe and then slower in its asymptotic decline off-axis. The half amplitude focal (pulse peak-based) beam widths for the

second harmonics were 0.62 and 0.60 of the corresponding fundamental half amplitude beam widths for the needle and Gaussian fields, respectively. This is less than the theoretical value of 0.71 (or  $1/\sqrt{N}$  for the Nth harmonic, here  $N=2$ ) (Hamilton and Blackstock, 1998a) for nonlinear beampatterns from a single frequency source. Figure 8(c) then shows the log-scaled version of the Fig. 8(b) data. With both of the needle source results, their slower off-axis sidelobe decline is visible, although the ultimate sidelobe levels are lower than their Gaussian peers. Note also that both the Gaussian and needle sources display significant sidelobe levels which are related to the source edge truncation.

Planar focal results are given in Figs. 9(a)–9(d). All of these figures display the peak amplitude pressures obtained in the  $r-z$  plane in a linear fashion. Figure 9(a) shows the radial planar peaks from the needle's fundamental band. Figure 9(b) depicts the corresponding Gaussian result. Figures 9(c) and 9(d) then show the corresponding second harmonic results from the nonlinearly propagated needle and Gaussian fields. In these results the lengthened axial focus of the needle source is apparent. Also displayed is the fact that the Gaussian field's sharp sidelobe decline [shown in Fig. 8(b)] is limited to close to the focal plane. The needle field's focal performance, on the other hand, appears to be relatively constant over the 1 cm of axial distance displayed.

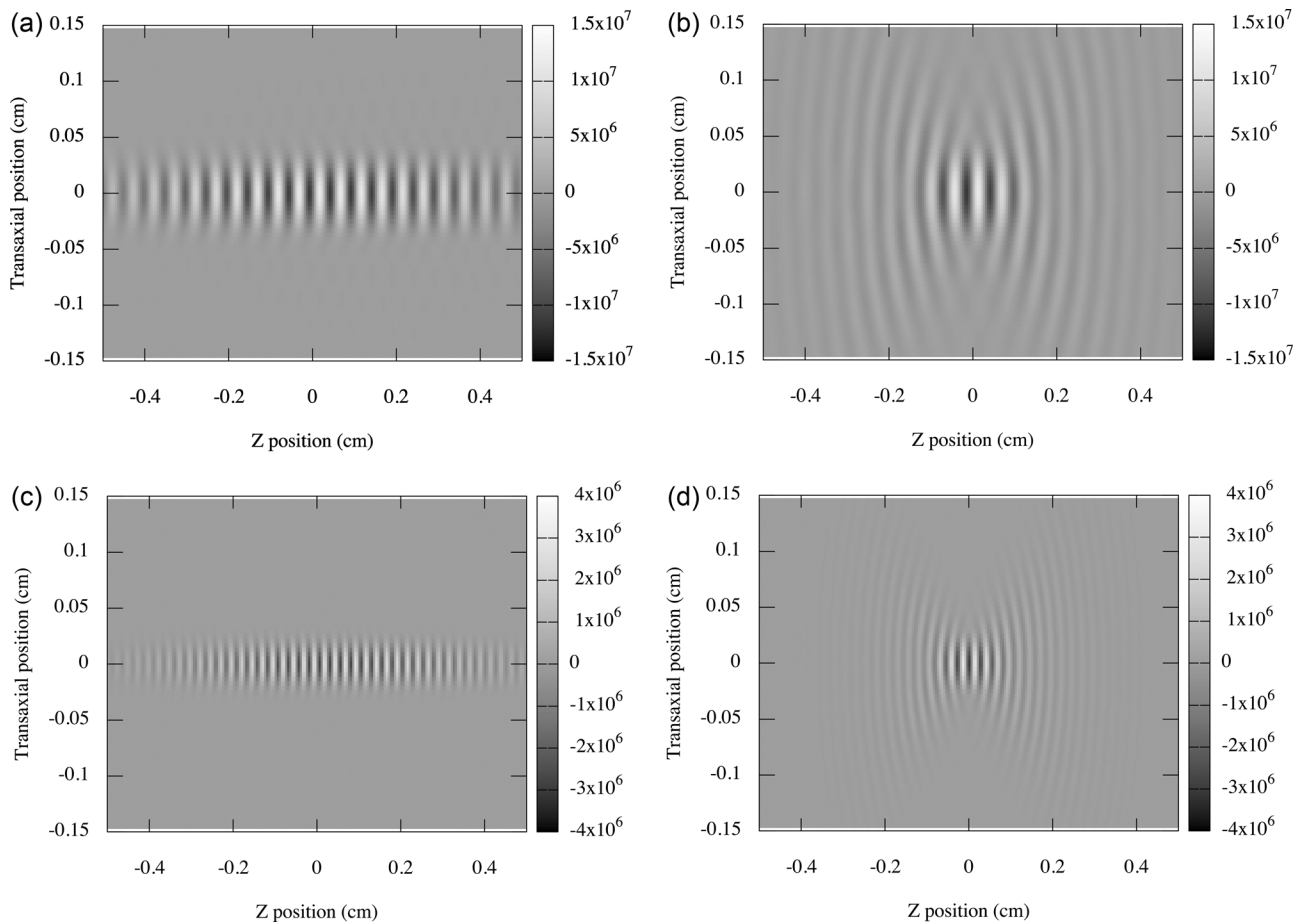


FIG. 10. The transaxial, fixed-time, pulse value planar results for the needle and Gaussian sources. All computations utilized the nonlinear model, but all figures here are linearly scaled. Note the reduced transaxial and axial range compared to Figs. 9(a)–9(d). (a) The planar pressure result computed from the needle field's fundamental bandwidth. (b) The corresponding result from the Gaussian's fundamental band. (c) The planar peak pressure result computed from the needle's second harmonic band. (d) The corresponding results from the Gaussian's second harmonic band.

Planar focal nonlinear results are depicted in Figs. 10(a)–10(d) for fixed time. The time used corresponded to the time of propagation to the focus, which was  $3\text{ cm} \div 0.15\text{ cm}/\mu\text{s} = 20\ \mu\text{s}$  (although that time corresponds to  $t = 0$  seconds in the needle field's formulation). All of these figures display in linear fashion the amplitude of the pulse at a given position in the  $r - z$  plane. Figures 10(a) and 10(b) show the fundamental-derived results for the needle and Gaussian results fields, respectively. Figures 10(c) and 10(d) depict the associated second harmonic-derived results for the needle and Gaussian results fields, respectively. The relatively sustained and stable form of the needle focal field is again apparent.

#### IV. CONCLUSION

We have compared a focused 3 MHz broadband Gaussian beam against a corresponding needle pulse field by utilizing the output of a nonlinear propagation model. These results suggest that the unique qualities of a needle focal field are inherited by their higher harmonic components. In particular, analogous to the fundamental linear needle pulse, the second harmonic characteristics include an extended needle-like, on-axis spatial peak, underlying shorter focal temporal pulses, and a narrower main lobe followed by a slower sidelobe decline.

The needle pulse's focal features—particularly the extended spatial focal peak and the shorter focal pulse lengths—may prove to be useful in some future applications where an extended depth of field and narrow beam width are advantageous.

#### ACKNOWLEDGMENTS

The work of K.J.P. was supported by the Hajim School of Engineering and Applied Sciences at the University of Rochester.

- Aanonsen, S. I., Barkve, T., Tjøtta, J. N., and Tjøtta, S. (1984). "Distortion and harmonic generation in the nearfield of a finite amplitude sound beam," *J. Acoust. Soc. Am.* **75**, 749–768.
- Baresch, D., Thomas, J., and Marchiano, R. (2016). "Observation of a single-beam gradient force acoustical trap for elastic particles: Acoustical tweezers," *Phys. Rev. Lett.* **116**, 024301.
- Brunet, T., Thomas, J., Marchiano, R., and Coulouvrat, F. (2009). "Experimental observation of azimuthal shock waves on nonlinear acoustical vortices," *New J. Phys.* **11**, 013002.
- Canney, M. S., Khokhlova, V. A., Bessonova, O. V., Bailey, M. R., and Crum, L. A. (2010). "Shock-induced heating and millisecond boiling in gels and tissue due to high intensity focused ultrasound," *Ultrasound Med. Biol.* **36**, 250–267.
- Christopher, P. T., and Parker, K. J. (1991a). "New approaches to nonlinear diffractive field propagation," *J. Acoust. Soc. Am.* **90**, 488–499.
- Christopher, P. T., and Parker, K. J. (1991b). "New approaches to the linear propagation of acoustic fields," *J. Acoust. Soc. Am.* **90**, 507–521.
- Christopher, T. (1994). "Modeling the Dornier HM3 lithotripter," *J. Acoust. Soc. Am.* **96**, 3088–3095.
- Christopher, T. (1997). "Finite amplitude distortion-based inhomogeneous pulse echo ultrasonic imaging," *IEEE Trans. Ultrason. Ferroelectr. Freq. Control* **44**, 125–139.
- Christopher, T. (2005). "HIFU focusing efficiency and a twin annular array source for prostate treatment," *IEEE Trans. Ultrason. Ferroelectr. Freq. Control* **52**, 1523–1533.
- Cleveland, R. O., Hamilton, M. F., and Blackstock, D. T. (1996). "Time-domain modeling of finite-amplitude sound in relaxing fluids," *J. Acoust. Soc. Am.* **99**, 3312–3318.
- Dagrau, F., Rénier, M., Marchiano, R., and Coulouvrat, F. (2011). "Acoustic shock wave propagation in a heterogeneous medium: A numerical simulation beyond the parabolic approximation," *J. Acoust. Soc. Am.* **130**, 20–32.
- Ding, D., and Liu, X. (1999). "Approximate description for Bessel, Bessel–Gauss, and Gaussian beams with finite aperture," *J. Opt. Soc. Am. A* **16**, 1286–1293.
- Du, G., and Breazeale, M. A. (1985). "The ultrasonic field of a Gaussian transducer," *J. Acoust. Soc. Am.* **78**, 2083–2086.
- Du, G., and Breazeale, M. A. (1986). "Harmonic distortion of a finite amplitude Gaussian beam in a fluid," *J. Acoust. Soc. Am.* **80**, 212–216.
- Du, G., and Breazeale, M. A. (1987). "Theoretical description of a focused Gaussian ultrasonic beam in a nonlinear medium," *J. Acoust. Soc. Am.* **81**, 51–57.
- Ginter, S., Liebler, M., Steiger, E., Dreyer, T., and Riedlinger, R. E. (2002). "Full-wave modeling of therapeutic ultrasound: Nonlinear ultrasound propagation in ideal fluids," *J. Acoust. Soc. Am.* **111**, 2049–2059.
- Hallaj, I. M., and Cleveland, R. O. (1999). "FDTD simulation of finite-amplitude pressure and temperature fields for biomedical ultrasound," *J. Acoust. Soc. Am.* **105**, L7–L12.
- Hamilton, M. F., and Blackstock, D. T. (1998a). *Nonlinear Acoustics* (Academic Press, San Diego, CA), Chap. 3.
- Hamilton, M. F., and Blackstock, D. T. (1998b). *Nonlinear Acoustics* (Academic Press, San Diego, CA), Chap. 8.
- Hefner, B. T., and Marston, P. L. (1999). "An acoustical helicoidal wave transducer with applications for the alignment of ultrasonic and underwater systems," *J. Acoust. Soc. Am.* **106**, 3313–3316.
- Hernández-Figueroa, H. E., Zamboni-Rached, M., and Recami, E. (2008). *Localized Waves* (Wiley-Interscience, IEEE Press, Hoboken, NJ).
- Hoffelner, J., Landes, H., Kaltenbacher, M., and Lerch, R. (2001). "Finite element simulation of nonlinear wave propagation in thermoviscous fluids including dissipation," *IEEE Trans. Ultrason. Ferroelectr. Freq. Control* **48**, 779–786.
- Huang, D., and Breazeale, M. A. (2006). "An ultrasonic Gaussian transducer and its diffraction field: Theory and practice," *IEEE Trans. Ultrason. Ferroelectr. Freq. Control* **53**, 1018–1027.
- Jing, Y., and Cleveland, R. O. (2007). "Modeling the propagation of nonlinear three-dimensional acoustic beams in inhomogeneous media," *J. Acoust. Soc. Am.* **122**, 1352–1364.
- Kenji, O., Shin, Y., and Shin-ichiro, U. (2012). "Therapeutic array transducer element using coresonance between hemispherical piezoceramic shell and water sphere: Effect of load masses of support and electric contact," *Jpn. J. Appl. Phys.* **51**, 07GF24.
- Lee, Y. S., and Hamilton, M. F. (1995). "Time-domain modeling of pulsed finite-amplitude sound beams," *J. Acoust. Soc. Am.* **97**, 906–917.
- Lu, J. Y., Zou, H., and Greenleaf, J. F. (1994). "Biomedical ultrasound beam forming," *Ultrasound Med. Biol.* **20**, 403–428.
- Marston, P. L. (2011). "Quasi-Gaussian beam analytical basis and comparison with an alternative approach (L)," *J. Acoust. Soc. Am.* **130**, 1091–1094.
- Parker, K. J., and Alonso, M. A. (2016). "Longitudinal iso-phase condition and needle pulses," *Opt. Express* **24**, 28669–28677.
- Parker, K. J., Chen, S., and Alonso, M. A. (2017). "The ultrasound needle pulse," *IEEE Trans. Ultrason. Ferroelectr. Freq. Control* **64**, 1045–1049.
- Pishchal'nikov, Y. A., Sapozhnikov, O. A., and Khokhlov, V. A. (1996). "A modification of the spectral description of nonlinear acoustic waves with discontinuities," *Acoust. Phys.* **42**, 362–367.
- Qiao, S., Jackson, E., Coussios, C. C., and Cleveland, R. O. (2016). "Simulation of nonlinear propagation of biomedical ultrasound using pzfex and the Khokhlov-Zabolotskaya-Kuznetsov Texas code," *J. Acoust. Soc. Am.* **140**, 2039–2046.
- Tavakkoli, J., Cathignol, D., Souchon, R., and Sapozhnikov, O. A. (1998). "Modeling of pulsed finite-amplitude focused sound beams in time domain," *J. Acoust. Soc. Am.* **104**, 2061–2072.
- Treeby, B. E., Jaros, J., Rendell, A. P., and Cox, B. T. (2012). "Modeling nonlinear ultrasound propagation in heterogeneous media with power law absorption using a k-space pseudospectral method," *J. Acoust. Soc. Am.* **131**, 4324–4336.
- Tripathi, B. B., Luca, A., Baskar, S., Coulouvrat, F., and Marchiano, R. (2018). "Element centered smooth artificial viscosity in discontinuous

- Galerkin method for propagation of acoustic shock waves on unstructured meshes," *J. Comput. Phys.* **366**, 298–319.
- Varslot, T., and Taraldsen, G. (2005). "Computer simulation of forward wave propagation in soft tissue," *IEEE Trans. Ultrason. Ferroelectr. Freq. Control* **52**, 1473–1482.
- Wen, J. J., and Breazeale, M. A. (1988). "A diffraction beam field expressed as the superposition of Gaussian beams," *J. Acoust. Soc. Am.* **83**, 1752–1756.
- Westervelt, P. J. (1963). "Parametric acoustic array," *J. Acoust. Soc. Am.* **35**, 535–537.
- Wojcik, G., Mould, J., Abboud, N., Ostromogilsky, M., and Vaughan, D. (1995). "Nonlinear modeling of therapeutic ultrasound," in *1995 IEEE Proceedings of the Ultrasonics Symposium*, pp. 1617–1622.
- Yuldashev, P. V., and Khokhlova, V. A. (2011). "Simulation of three-dimensional nonlinear fields of ultrasound therapeutic arrays," *Acoust. Phys.* **57**, 334–343.
- Zabolotskaya, E., and Khokhlov, R. (1969). "Quasi-plane waves in the nonlinear acoustics of confined beams," *Sov. Phys. Acoust.* **15**, 35–40.